



Research paper

A parallel-guided compliant mechanism with variable stiffness based on layer jamming

Xianpai Zeng^a, Cart Hurd^a, Hai-Jun Su^{a,*}, Siyang Song^b, Junmin Wang^b^a Mechanical and Aerospace Engineering, The Ohio State University, Columbus, OH 43210, United States^b Mechanical Engineering, University of Texas at Austin, TX 78712, USA

ARTICLE INFO

Article history:

Received 2 October 2019

Revised 2 January 2020

Accepted 3 January 2020

Available online 3 February 2020

Keywords:

Parallel-Guided

Compliant Mechanisms

Variable Stiffness

Layer Jamming

ABSTRACT

This article introduces a parallel-guided compliant mechanism, which can achieve a high stiffness ratio (maximum over minimum) of 75 times through pneumatic actuated layer jamming. The compliant mechanism is composed of two flexible beams sandwiched with thin plastic friction layers. With a novel beam cross-section, the beams have large thickness, but still retain high flexibility. The effect of layer jamming is augmented by this large thickness due to the increased leverage of friction force. The beams in parallel-guided configuration have higher vertical and torsional stability compared to a single beam setup. The functionalities of the compliant mechanism have been validated experimentally: stiffness is measured as a function of the applied vacuum pressure. This paper describes the design concept, FEA validation of the design concept, prototyping, experiment results, analytical model, and analysis of vertical and torsional stability. The proposed concept of the compliant mechanism provides a potential solution for design of variable stiffness robotic links for addressing safety concerns in physical human robot interaction. The analytical model for identifying critical design parameters for maximum stiffness-variation effect provides a guideline for high stiffness-variation design on similar structures.

© 2020 Elsevier Ltd. All rights reserved.

1. Introduction

Compliant robots, robots that have inherent compliance, offer alternative solutions to numerous complex tasks that requires a high degree of freedom. Compliant robots are typically constructed from materials such as textiles, elastomers, or any other highly flexible materials. Due to the materials' flexibility and theoretically infinite degree of freedom, compliant robots can be extremely dexterous, and less likely to damage fragile payloads or injure humans [1,2]. Compliant robots can also be less expensive, lighter weight, and easier to customize for different applications [3].

However, there are some limitations associated with their high compliance. One challenge with compliant robotics is to obtain high positional accuracy. Their inherent flexibility makes it difficult to control the exact position of the robots appendages. The theoretically infinite degree of freedom makes it a challenge for applying sensor setups such as encoders. Additionally, compliant robots tend to have large deformation under external loads. This prevents compliant robots from matching the load-carrying capabilities of traditional rigid counterparts.

Due to the performance limitations of compliant robots, interest has risen in exploring variable stiffness technologies. Robots with control over their stiffness could potentially possess both the advantages of compliant robots and the high

* Corresponding author.

E-mail address: su.298@osu.edu (H.-J. Su).

performance of rigid ones. A robot capable of varying its stiffness can become more rigid when higher positional accuracy or load capabilities are needed, but can also become compliant to avoid injuring humans. For robots in assistive, rehabilitative, and domestic roles, safety is a critical design concern. The safety issue must be addressed before robots can work closely with humans.

Extensive studies have been conducted on variable stiffness technologies. Blanc et al. [4] classified controllable stiffness mechanisms on the basis of change in intrinsic properties. The solution for the first main family is to change the second moment of the area. The second main family's solution is to change the material-related elastic properties, e.g. elastic modulus, either by utilizing tunable material properties (material-based solutions) or by controlling the structural interactions (locking-based solutions). As an example of the solutions from the first family, She et al. [5] built a 1R robotic arm with active stiffness control by altering the shape of the cross-section. This design allows for a change in stiffness by 3.6 times. However, the actuation mechanism, including servo motors, linkages, and bearings adds complexity and introduces new points of failure. Most of the latest solutions fall into the second family. Lower melting-point polymers and magnetorheological materials are two representative material-based solutions. The method using low melting point polymers can produce a fairly high stiffness ratio (> 25 times). Nonetheless, experiments suggest that this variable stiffness method is not durable enough to handle high loads and impacts [6]. Magnetorheological material-based technology has been used to adjust the spring constant of vibration absorbers in real time for better vibration isolation. However, at this time the technology is not ideal for structural parts [7].

Increasing attention has been drawn to locking-based solutions. Methods that control the interactions of locking elements are categorized as jamming solutions. Most jamming structures consist of a sealed volume, filled with locking elements, usually either a granular, fiber, or sheet material. Friction force among the locking elements is related to the applied force or pressure. The structure's stiffness can be controlled as the result this tunable interaction. Granular jamming has been studied and used to create robotic joints [8] and manipulators [9–13]. Fiber jamming has been studied in terms of fibers' elastic properties, arrangement, geometrical features, and surface roughness [14]. However, these designs have relatively low stiffness ratio. In contrast, layer jamming has shown potential for achieving high stiffness ratio. Layer jamming has been used in applications requiring high strength, such as a stool which can support a persons weight [15]. Kim et al. [16,17] developed a manipulator using layer jamming for minimally invasive surgery. The manipulator can assume a flexible state for insertion without accidental injury and a stiff state for high positional accuracy. Langer et al. [18] proposed a stiffening sheath for tendon-actuated continuum robots. The bending stiffness is improved by a factor up to 24. However, the stiffness variation on the continuum robot arm negatively affects its load-carrying capability. Due to its circular cross-section design, the compliance is also introduced in its loading direction causing stiffness variation coupled with its load-carrying capability. A rapid stiffness change from high to low would cause undesirable deflection or even collapse under vertical load. To address this issue, selective stiffening is studied on a sandwich-like stiffened structure which achieved the stiffness ratio of 8 [19]. The latest studies and applications of layer jamming are focused more on finding new designs of backbone on which jamming layers are attached, [20,21], or exploring appropriate medical application scenarios [22–24]. The early and latest studies and applications of layer jamming lack discussion on design guidelines based on analytical models. Designing for high stiffness ratio and quick response remains a challenge.

In this paper, we propose a compliant mechanism solution for achieving a large stiffness ratio with quick response and high stability. The rest of paper is organized as the following. In Section 2, the conceptual design and hypotheses are introduced. In Section 3, a quasi-static model is developed. Design parameters are identified. In Section 4, the design concept is verified with a finite element analysis. In Section 5, sensitivity analysis based on the lumped-parameter model are conducted to explore the effects of the identified design parameters. In Section 6, the experimental evaluation of the design based on a prototype is introduced.

2. Motivations and design overview

Introducing compliance to robotic structures is a well-known method for addressing safety concerns in physical human-robot-interactions. However, compliance could reduce the performance (positioning accuracy and control bandwidth etc.) of the robot. Employing variable stiffness has been extensively studied for address the trade-off between these two competing metric: performance and safety. An ideal variable stiffness solution should satisfy four main criteria: large stiffness ratio, quick response, high stability and low design overhead (system complexity or extra weight). Here stiffness ratio is defined as “the ratio of high stiffness over low stiffness”. The current variable stiffness solutions rarely satisfy all of these four criteria.

In this work, we propose a novel parallel-guided compliant mechanism combined with pneumatic-actuated layer jamming for stiffness varying. As shown in Fig. 1(a), the design features two flexible beams connected in parallel with one end being clamped and the other end being free. Upon application of external load, the free end tends to move laterally with the fixed end, Fig. 1(b). Each beam is formed by a series of small flexure hinges, sandwiched with 4–8 sheets of jamming layer materials on both sides and sealed in an air-tight bag, Fig. 1(c). Our hypothesis is that (1) large stiffness ratio can be achieved by combining layer jamming with flexible-backbone design, (2) high vertical and torsional stability can be achieved by using the parallel-guided beam configuration.

The functioning of the design is described as the following. The sealed bag is connected to a vacuum pump via tubing. When the air in the bag is vacuumed out, the air pressure applied to both sides of beams generates friction between layers,

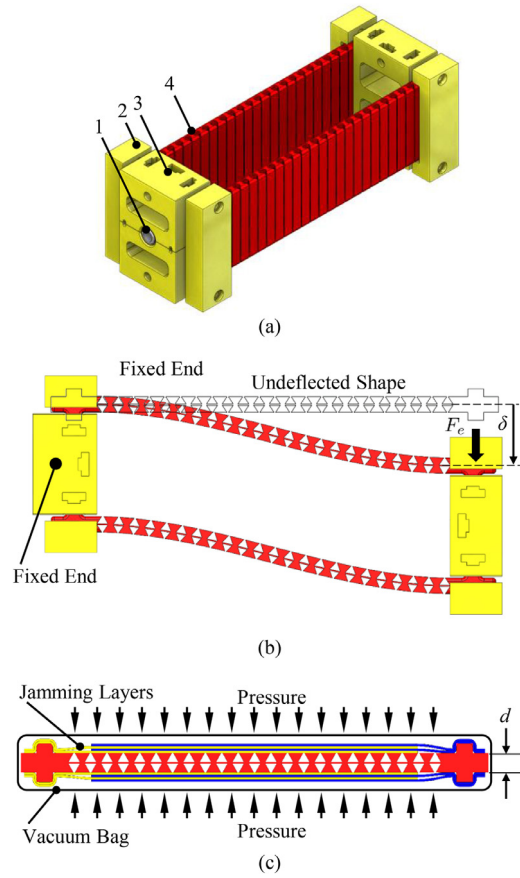


Fig. 1. Design Overview. Details of the proposed parallel-guided compliant mechanism. (a): An isometric view of the parallel-guided compliant mechanism showing (1) push-to-connect vacuum inlet, (2) beam holder, (3) end block (4) flexible beam (b) The distal end moves laterally due to the parallel-guided constraints. (c) Two sets of interleaved jamming layers are attached to the beam and encapsulated in the vacuum bag.

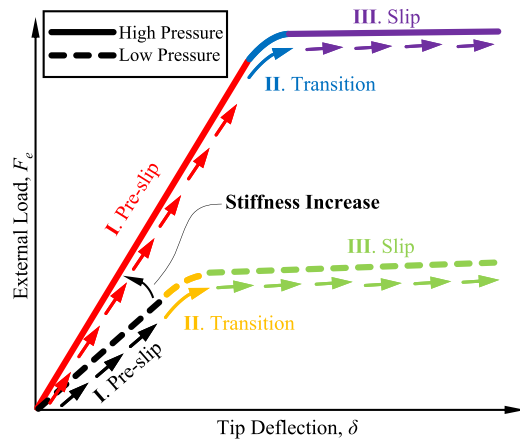


Fig. 2. Schematic Illustration of Loading Phases. Phase I: Pre-slip phase. Phase II: Transition phase. Phase III: Slip phase.

hence preventing the beam from bending. As shown in the schematic diagram (Fig. 2), the mechanism undergoes three basic phases upon application of external load applied the free-end. In Phase I (Pre-slip Phase), under low external load, the initial stiffness remains constant. In Phase II (Transition Phase), the stiffness begins to decrease gradually under increased external load. In Phase III (Slip Phase), the stiffness reaches a saturated value with even larger and increased external load. The transitional external load, the load under which the stiffness starts to decrease from the initial linear stiffness, is related to the applied vacuum pressure. Higher vacuum pressure leads to a larger transitional external load. The saturated stiffness,

which is the final linear stiffness, is independent of the applied vacuum pressure as estimated from the slopes of the final linear region. This is caused by the fully slip of the jamming layers. This behavior is also observed in jamming structures in single-stack configuration [25,26].

This dual-beam configuration has several advantages over a single-beam setup. First, maximum stiffness is greater than that of a single beam. This is not only due to the increased number of beams and friction layers, but also due to the end constraints imposed on the deflecting end. Second, the dual-beam configuration has much higher vertical and torsional stability compared to the single-beam configuration. Both beams are made with flexible material. The compliant backbone serves two purposes: (1) to significantly increase the mechanism's stiffness ratio since the backbone structure has a large thickness leveraging resistance moment resulted from friction forces in jamming layers, (2) to restore the mechanism to its undeflected shape upon releasing the vacuum pressure. Fig. 1(b) shows the interlocked arrangement of jamming layers. The interlocked-layer configuration is tested to have better performance with respect to obtaining high stiffness ratio than granular jamming and fish-scale-like configuration [19]. The top and bottom surfaces of the hourglass-shaped structures provide "supporting surfaces" for jamming layers, yet have minimal negative impact on the lateral flexibility of the beam. The beam bends under lateral load, which is exemplified by rotations of hourglass-shaped features. The rotation of each hourglass-shaped feature can be resisted by the moment generated by the friction forces on its top and bottom surfaces. Two stacks of layers, on the top and bottom surfaces respectively, are separated by a larger distance, d (illustrated in Fig. 1(c)), compared to a single stack of layers. The leverage of friction forces are increased by this distance, d . Thus, jamming effect is enhanced. The hourglass-shaped structures also act as stiffeners which leads to significantly higher vertical and torsional stability. The size of the openings among the hourglass-shaped structures needs to be selected with close attention. The range of motion can be limited by interference whenever the two structures are positioned too close together. On the other end, if the hourglass-shaped structures are spaced too far apart, the unsupported portion of jamming layers tend to buckle when the mechanism is under a lateral load, which would significantly decrease the mechanism's lateral stiffness.

3. Mechanics and stiffness modeling

For the proposed design, the stiffness only varies in the lateral direction. The lateral tip deflection is expected to have a nonlinear relationship with the lateral external load. Hence, the lateral stiffness corresponding to an instantaneous lateral deflection, δ , is defined as

$$k = \frac{dF_e}{d\delta}, \quad (1)$$

where F_e is the external load, illustrated in Fig. 1(b). Subsequently, the stiffness ratio is

$$n_k = \frac{k_h}{k_l}, \quad (2)$$

where k_h and k_l are the highest and lowest stiffness the prototype could achieve, respectively.

In Phase I, all of the jamming layers are pressed against the flat surfaces of hourglass-shaped structures under the applied vacuum pressure. The jamming layers and beams are cohesive, behaving as a single beam. In Phase I, the parallel-guided mechanism obtains maximum stiffness. In Phase II, slippage begins to occur between jamming layers. This is because the local friction force, which restrains the rotation of the hourglass-shaped structures, exceeds the maximum friction force that the jamming layers can produce. The slippage initially begins from the ends of the beam and propagates toward the center under increased external load. In Phase III, the slippage propagates through out the center of the beam. The friction force between layers can be modeled as dynamic friction since all of the layers are slipping. In this region, the stiffness reaches its minimum and constant value.

It is imperative to develop a method to find the wavefront of the slippage propagation, or the slippage boundary, χ . The beam is modeled as a combination of discrete flexible and rigid sections. The geometric dimensions used in the analytical modeling is shown in Fig. 3.

At the i th section, the moment generated by the local friction force

$$M_i = \frac{F_e}{2} \left(\frac{L_b}{2} - x_i \right) - F_f d \quad (1 \leq i \leq n), \quad (3)$$

where F_f , illustrated in Fig. 3(b), is the friction force exerted on the top and bottom surfaces of one hourglass-shaped structure by jamming layers. F_e , shown in Fig. 1(b), is the total external lateral force on the distal end of the mechanism. Then the deflecting angle at the end of the i th flexible section can be expressed as

$$\theta_i = \frac{M_i l}{(EI)_e}. \quad (4)$$

The parallel-guided compliant beam is proposed as a potential solution for impact reduction by using its large stiffness ratio. During the impact, the lateral deflection of the distal end of the beam is very small compared to its length. For this design, we expect a deflection that is less than 20 mm on a prototype that has an length of 227 mm. The curvature of each hourglass-shaped section is minimal. Therefore it is assumed that $\sin(\theta) = \theta$. Thenthe combined deflection of the i th

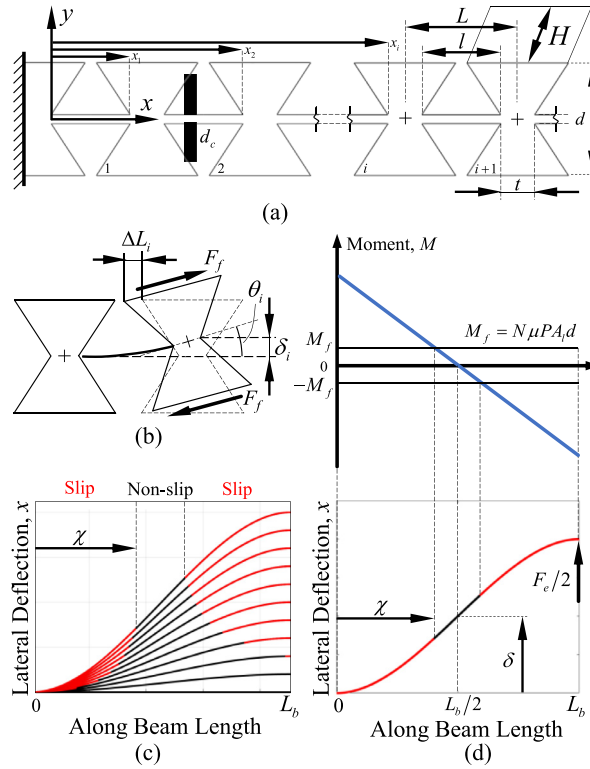


Fig. 3. Lumped Parameter Model Setup and Schematic. (a) Geometric parameters on undeflected beam. (b) Geometric parameters on deflected beam. (c) Illustration on the definition of χ . (d) Moment distribution along the beam length.

flexible and rigid sections is

$$\delta_i = \theta_i \left(\frac{l}{2} + t \right) + L \sum_{j=1}^{i-1} (\theta_j). \tag{5}$$

The total deflection of the whole beam is the summation of the deflections of all of the n sections.

$$\delta = \sum_{i=1}^n \delta_i = \sum_{i=1}^n \left(\theta_i \left(\frac{l}{2} + t \right) + L \sum_{j=0}^{i-1} (\theta_j) \right) \quad (\theta_0 = 0).$$

The jamming layers are stretched under the in-plane friction force. The strain in the layers is

$$\epsilon_l = \frac{F_f}{NE_l A_x}. \tag{6}$$

Strain at the surface of the beam is

$$\epsilon_b = \frac{\Delta L_i}{L} = \frac{\theta_i d}{2L}. \tag{7}$$

The boundary between slipped layers and bonded layers needs to be determined, since different governing laws are applied to each region. When vacuum pressure is applied, layers are pressed against adjacent layers or surfaces. Under zero external force, layers are treated in the way that all surfaces are bonded. When external load begins to increase, the beam begins to bend with larger curvatures at both clamped ends, as shown in Fig. 3(c). The largest moment generated by the local friction force is $\mu PA_1 d$. When the local moment caused by the external load exceeds this maximum value, the residual moment has to be balanced by the bending of the beam, which is the reason that larger curvature is observed at both ends. The region within which the moment caused by the external load is larger than or equal to the moment generated by the local friction force is referred to as the “slip region”, the rest of the layer as “non-slip region”. With increasing external load, the slip region tends to propagate toward the center of the beam. This is shown by the expanding length of the red curves corresponding to increasing external load in Fig. 3(c). The boundary between the slip region and non-slip region is characterized by χ , which is the length measured along the beam length from one clamped end to this boundary. The value of χ

is obtained by matching the strain in the jamming layers and the strain on the surface of the beam. By enforcing $\epsilon_l = \epsilon_b$, the expression of χ is

$$\chi = \frac{1}{2}L_b - 4\frac{\mu PA_l}{F_e} \left(\frac{1}{2}d + \frac{1}{d} \frac{L_i}{l_i} \frac{(EI)_e}{NE_l A_x} \right). \quad (8)$$

Combining the result, the expression of total deflection of the mechanism is

$$\delta = \sum_{i=1}^n \left(\frac{\frac{1}{2}F_e \left(\frac{L}{2} - x_i \right) - F_f d}{2(EI)_e} l^2 + t\theta_i + L \sum_{j=0}^{i-1} (\theta_j) \right) \quad (9)$$

where

$$F_f = \begin{cases} \mu PA_l & 0 \leq x_i \leq \chi \\ \frac{1}{4}d \frac{l_i}{L_i} \left(\frac{L_b}{2} - x_i \right) F_e & \chi < x_i \leq \frac{L_b}{2} \\ \frac{1}{2}d^2 \frac{l_i}{L_i} + \frac{(EI)_e}{NE_l A_x} & \end{cases} \quad (10)$$

and

$$(EI)_e = \begin{cases} E_b I_b + E_v I_v + 2NE_l I_l & 0 \leq x_i \leq \chi \\ E_b I_b + E_v I_v + 2N^3 E_l I_l & \chi < x_i \leq \frac{L_b}{2} \end{cases} \quad (11)$$

4. Validation with finite element simulations

To validate the design's variable stiffness capability and its stability, an FEA model was built in ANSYS 19.2 Workbench. Fig. 4(a) shows the FEA model setup. Since the stiffness of the hourglass-shaped sections is much higher than that of the thin flexible sections, all of the hourglass-shaped sections are set to have rigid stiffness behavior. Shell elements are used to model the flexible sections, jamming layers, and vacuum membranes. Mesh size is set to be 2 mm based on convergence studies on stresses in flexible beams, jamming layers, and vacuum membranes. Frictional contact pairs are configured between the backbone and the bottom jamming layer, between the jamming layers, and between the outermost jamming layers and their corresponding vacuum membranes. A coefficient of friction of 0.167 is used based on experimental measurement of the jamming layers. Augmented Lagrange is enabled for contact formulation. Relevant motion between layers is visible in Fig. 4(b). The distribution of normal elastic strain on the bottom layer, which has direct contact with the backbone, is illustrated in Fig. 4(c). Zero normal strain is observed in the middle span of the layer. Both normal strain and shear strain are plotted on the path along the longitudinal direction in Fig. 4(d). Normal strain is relatively constant at the beginning of the path, then decreased linearly along the longitudinal direction. Shear strain is minimal, compared to normal strain.

4.1. Stiffness Variation

The load-displacement curves under various vacuum pressures are plotted in Fig. 4(e). With 0 psi gauge vacuum pressure, a linear load-deflection relationship is observed, indicating constant stiffness. Once vacuum is applied, three distinct phases of stiffness-increase are observed.

The geometry and material properties are based on the actual prototype and listed in Table 1. The geometric-nonlinearity and boundary-nonlinearity nature of the simulation incur high computational cost. In addition, the modeling complexity is also high, due to the large amount of contact pairs. The two main drawbacks, when combined, make the FEA model incapable of predicting the behavior of the proposed design based on various design parameters. It is necessary to have a lumped-parameter model that also uses actual geometric and physical parameters, but can significantly reduce the computational complexity.

4.2. Critical vertical buckling load

One of the concerns on compliant mechanism is the stability under vertical and torsional loads. The proposed parallel-guided compliant mechanism is designed to significantly increase the stability under vertical and torsional loads, while maintaining flexibility in the lateral direction. In this section, critical vertical buckling load (CVBL) is first discussed in three configurations, including single uniform plate, dual uniform plates, and the proposed dual beams with hourglass-shaped structures, as shown in Fig. 5(a). The effects of beam thickness and the distance between the dual beams are investigated. Then the torsional stability is analyzed.

Compliant mechanisms can fail due to yielding or buckling. To determine the their weight-carrying capability, both failure modes need to be considered. Compared to rigid mechanisms, compliant mechanisms tend to have excessive deflection under the same load. This is caused by the softer materials or redundant degrees of freedom that most compliant mechanisms utilize. The excessive deflection leaves compliant mechanisms vulnerable to buckling. As shown in Fig. 5(a), an FEA study is conducted on three configurations under a vertical end load. In both single and dual cases, the rectangular plate is

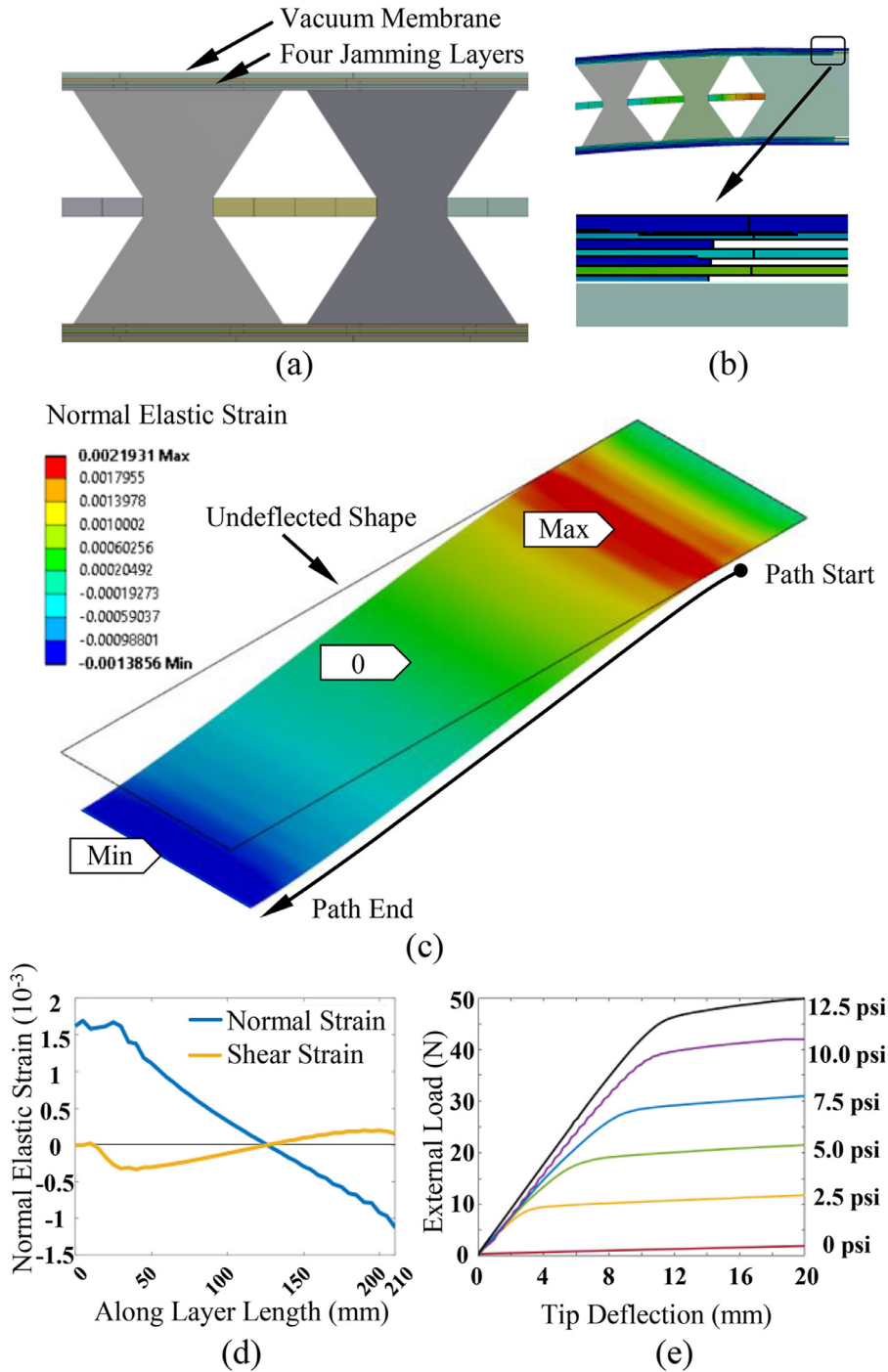


Fig. 4. FEA Model Setup and Results. (a) FEA configuration on the backbone, jamming layers and vacuum membranes. (b) Relative motion between layers under external load. (c) Normal elastic strain distribution. (d) Normal and shear elastic strain along the path. (e) Load-displacement curves corresponding to various vacuum pressures.

straight and uniform. To resemble the proposed prototype, rigid sections are added to simulate the hourglass-shaped structures. The cross-section shown on the right of Fig. 5(a) is for the cases of “Single Uniform”, “Dual Uniform”, and the flexible sections in “Dual w/ Stiffeners”. For the single-plate configuration, the CVBL can be estimated both analytically [27, p. 728] and by FEA. Buckling modes presented in Fig. 5(b) suggest that the upper distal corner of the single plate where the load is applied deflects sideways, resulting in a low CVBL (0.79 N). This occurs long before the material’s yield strength has been

Table 1
Model constants

Symbol	Description	Value
Key Design Parameters		
N	Number of frictional layers on each side	4
H	Beam height	75 mm
d	Beam thickness	10 mm
d_c	Center beam thickness	0.8 mm
Material Parameters		
E_l	Modulus of layer material	2.6 GPa
E_b	Modulus of beam material	4.0 GPa
E_v	Modulus of vacuum membrane material	0.02 GPa
μ	Friction coefficient	0.167
Beam Dimensions		
L_b	Beam length	227 mm
l	Length of flexible part of one unit	7 mm
t	Length of rigid part of one unit	3 mm
L	Total length of one unit	10 mm
n	Total number of unit sections	23

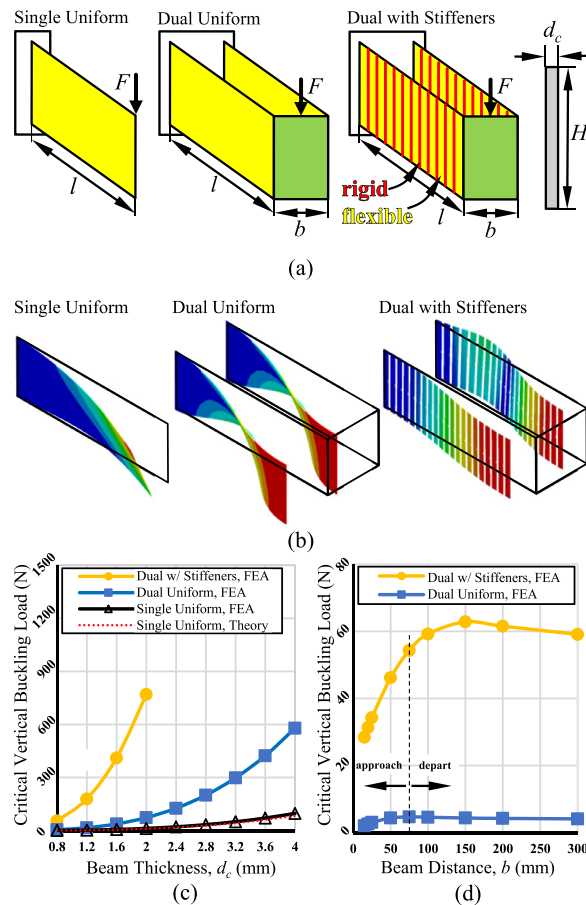


Fig. 5. Studies on CVBL. (a): Three beam configurations: single uniform plate, dual uniform plates, and dual plates with stiffeners. (b): Buckling modes. (c): Effect of beam thickness, d_c , on CVBL. (d): Effect of beam distance, b , on CVBL.

reached. The dual-plate configuration also fails due to buckling, but with a higher CVBL (4.70N). This is due to the guided boundary condition on the distal end that contains the upper corner from deflecting excessively. With rigid sections added, the CVBL is significantly increased to 54.3 N. This may be due to the deflection of flexible sections being restrained by the adjacent rigid ones. On the prototype, this feature is realized by the hourglass-shaped structures. They act as stiffeners that help to obtain high vertical stability, but retain high flexibility in the lateral direction.

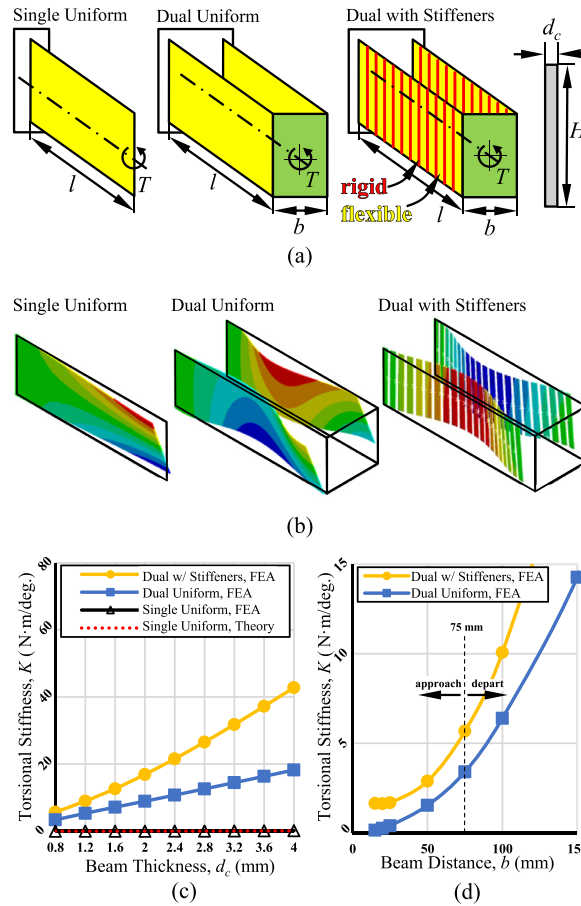


Fig. 6. Studies on torsional stiffness. (a): Three beam configurations: single uniform plate, dual uniform plates, and dual plates with stiffeners. (b): Deflection diagrams. (c): Effect of beam thickness, d_c , on torsional stiffness. (d): Effect of beam distance, b , on torsional stiffness.

The effects of beam thickness, d_c , and beam distance, b , on CVBL are analyzed. Fig. 5(c) suggests that the vertical stability can be significantly increased with a thicker center beam in all three cases. In the case of dual beams with stiffeners, the CVBL is increased to about 800 N with a beam thickness variation of up to 2 mm. At this point, the maximum von Mises stress reaches yield strength. If the beam thickness is further increased, the mechanism is expected to fail due to yielding. It is worth noting here that larger beam thickness has a negative impact on stiffness ratio as previously shown in the design studies herein. To explore the role that the beam distance, b , plays in the vertical stability, the distance is first varied from 75 mm down to 15 mm. With decreased distance, the dual beams will eventually merge into a single beam, thus reducing the vertical stability. This is exemplified in Fig. 5(d), by the reduced CVBL with the beams approaching each other. Next, the beam distance is increased from 75 mm to 300 mm. In this case, the vertical stability is not affected as effectively as by decreasing the beam distance. The result indicates that vertical stability can be optimized with a well-selected beam distance, b .

4.3. Torsional Stiffness

Any load carried by the end effector, if not precisely above the central axis of the mechanism, can cause rotation along this axis. Compliant mechanisms tend to have lower torsional stiffness compared to rigid ones. Their ability to resist torque thus needs to be considered.

As shown in Fig. 6(a), the same FEA model, with load changed to a torque along the longitudinal axis, is used to study the mechanism's torsional stability. It is worth noting that the end of the mechanism is free to translate along the longitudinal direction on all three cases, i.e., the mechanism length could change under torsional load. Fig. 6(b) displays the deflection diagrams of all three cases. The single uniform plate twists along its longitudinal axis. This is a typical case of pure torsion on a bar with a rectangular cross-section. The torsional stiffness can be theoretically estimated [27, p. 401]. Both FEA and the theoretical results of the torsional stiffness on the single uniform plate are presented in Fig. 6(c) by the red dotted curve and black curve with triangular markers, respectively. The single uniform plate has low torsional stiffness due to small thickness

($d_c = 0.8$ mm), low modulus of elasticity ($E = 2.6$ GPa), and the free-to-twist boundary condition. The dual uniform plates exhibit a twist-and-bend combined deformation. The guided constraint prevents the beam's cross-section from displacing axially during twisting. This implicates that the dual-beam is under warping torsion, meaning that the applied torque is carried by axial stresses in addition to shear stresses. With the stiffeners added, even more torque is carried by axial stresses as exemplified by the inward-bending shape.

Similarly, the effects of beam thickness, d_c , and beam distance, b , on torsional stiffness have been studied. The results are presented in Fig. 6(c) and (d). As discussed above, the single plate has a very low torsional stiffness of $K_{su} = 0.0013 \text{ N} \cdot \text{m}/\text{deg}$. estimated by FEA, although it increases with the beam thickness, d_c . Both dual uniform plates and dual plates with stiffeners follow the same trend, but with significantly higher torsional stiffness. At $d_c = 0.8$ mm, which is the thickness of the center beam on the prototype, the torsional stiffness of dual uniform plates and dual plates with stiffeners are $K_{du} = 3.48 \text{ N} \cdot \text{m}/\text{deg}$. and $K_{ds} = 5.68 \text{ N} \cdot \text{m}/\text{deg}$., respectively. The added stiffeners almost double the torsional stiffness. If the designed vertical load, $m_{load} = 5$ kg, were to be placed entirely on one beam instead of placed above the central axis, the twist angle of the mechanism would be calculated as

$$\theta_{twist} = \frac{(m_{load})g(0.5b)}{K_{ds}} = 0.32\text{deg}., \quad (12)$$

where $g = 9.8 \text{ N}/\text{kg}$, $b = 0.075$ m, which is the beam distance. The twist angle can be neglected even for this extreme scenario. Now while keeping the beam thickness constant at $d_c = 0.8$ mm, the distance between the two beams is varied. With the beams approaching each other, torsional stiffness decreases since the high torsional stability will eventually vanish with the two beams merging into one. By the same token, the torsional stiffness increases with the beams moved further apart.

This result demonstrates the advantage of parallel-guided configuration in obtaining high vertical and torsional stability.

5. Sensitivity analysis on key design parameters

Design parameters are identified in Table 1 and illustrated in Fig. 3(a). The geometric design parameters include the number of jamming layers N , the beam thickness d , the center beam thickness d_c , and the beam height H . The material design parameters include the elastic modulus of the beam material E_b , and the elastic modulus of the layer material E_l . In this section, the effects of these design parameters on stiffness ratio are studied.

The results of the sensitivity analysis are plotted in Fig. 7. The colored contours stand for stiffness ratio which is predicted corresponding to the presented parameters. The cross indicates the parameters of the current design. The arrow points to the direction in which a larger stiffness ratio could be achieved. From these plots, we can draw the following conclusions.

1. Higher modulus of layer material and lower modulus of the beam material lead to a greater stiffness ratio. This greater stiffness ratio can be attributed to the greater high stiffness, which is the result of the higher modulus of layer material, and the lesser low stiffness, which is the result of the lower modulus of the beam material. See Fig. 7(a).
2. Increasing the number of layers leads to higher stiffness ratio. This is caused by greater high stiffness. See Fig. 7(b).
3. The stiffness ratio would be almost doubled if the beam thickness were increased from 10mm to 20mm. The sensitivity of stiffness ratio is high on beam thickness, which is the key design parameter of the proposed design. This positive correlation is also due to the greater high stiffness obtained by larger beam thickness. See Fig. 7(c).
4. Both beam height and center beam thickness are negatively correlated to the stiffness ratio. Decreasing both beam height and center beam thickness could lead to very great stiffness ratio; however this would cause greater maximum stress, which may impact the load-carrying capability of the proposed design. Caution needs to be exercised when decreasing the beam height and center beam thickness. See Fig. 7(d).

The number of jamming layers could be modified during the fabrication process before the vacuum membrane is sealed. Beam thickness, height, and center beam thickness could be changed by prototyping a replacement beam with new dimensions. The adjustment of material parameters would have to be through replacing the material. The elastic modulus of the layer material could be changed by selecting a different sheet material.

6. Prototype and experimental testing

6.1. Fabrication process and prototype

The design aims to replace the robotic links on industrial robot that handles medium-duty tasks (5 kg payload) such as UR5. The dimensions are determined in the way that the prototype can replace one of the rigid robotic links without major revisions.

Fig. 8 shows the CAD model of the beam which is 3D-printed as a single part on Makerbot Z18 with polylactic acid (PLA) filament. 3D-printing played a major role in accelerating design iterations, through which the final hourglass-shaped features and the dimensions are obtained. However, the manufacture method of the beam is not limited to 3D-printing. 3D-printing is declared only to present the fabrication method we used. A discussion on the optimal (most cost-effective) manufacturing method may be necessary if production manufacturing is needed. But it is out of the scope of this work.

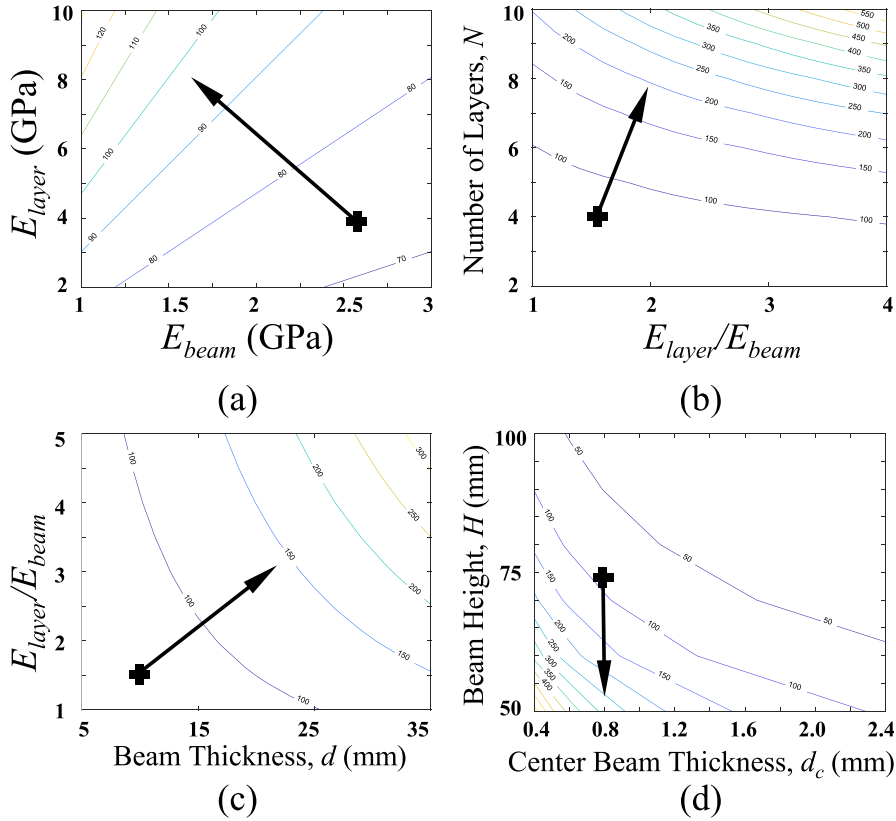


Fig. 7. Sensitivity study has been done on various geometric and material parameters, such as (a) moduli of friction layer material and beam material, (b) number of layers and moduli ratio, (c) number of layers and beam height, and (d) beam height and center beam thickness. Design parameters are identified in Table 1 and illustrated in Fig. 3(a). The geometric design parameters include the number of jamming layers N , the beam thickness d , the center beam thickness d_c , and the beam height H . The material design parameters include the elastic modulus of the beam material E_b , and the elastic modulus of the layer material E_l .

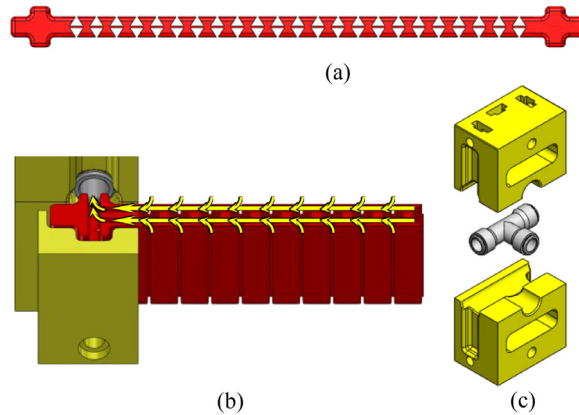


Fig. 8. Details of the proposed parallel-guided compliant mechanism. (a): beam with hourglass-shaped features. (b): internal air channels that facilitate quick air flows. (c): Exploded view of the end block components showing the embedded push-to-connect vacuum inlet.

For fast response, air needs to be removed from the vacuum bag quickly. As shown in Fig. 8(b), channels as an internal feature of beams have been designed to facilitate fast air removal. The internal air channels are made during the 3D-printing, with no extra fabrication process needed. The other measure for quick actuation is to use a high-flow-rate vacuum generator rather than motor-based vacuum pumps. A push-to-connect inlet (Fig. 8(c)) connects both beams to the vacuum generator.

The fabrication process is shown in Fig. 9. Jamming layers are cut from 0.005 in. thickness (0.127mm) Dura-Lar film on a laser-cut machine. Permanent adhesive is used to attach the jamming layers to the beams. The vacuum membrane is made

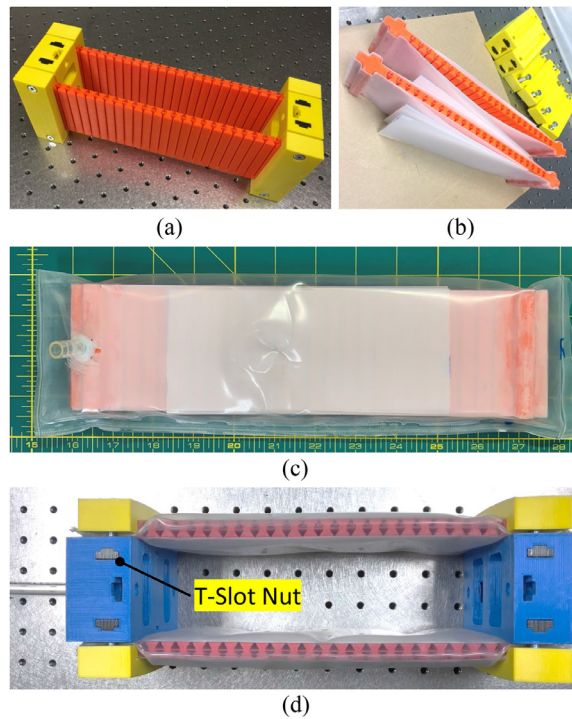


Fig. 9. Fabrication process. (a) 3D printed parts are assembled to test fitting. (b) Jamming layers are bonded to ends of beams with permanent adhesive. (c) Vacuum bag is made by heat sealing of polyurethane film. (d) Final assembly.

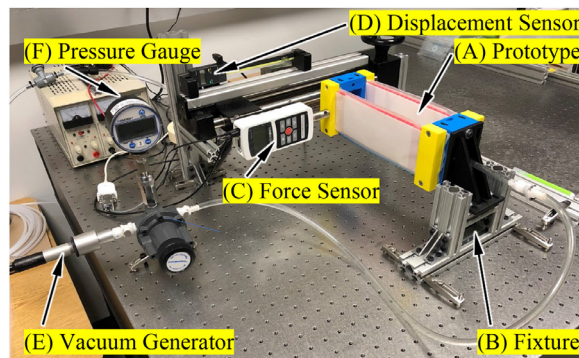


Fig. 10. Experiment Setup. The parallel-guided compliant mechanism (A) is fixed to the base (B) which is assembled using aluminum frames to ensure a rigid base fixture. Force and deflection are collected using Mark-10 measurement gauge which incorporates a force sensor (C) and a deflection sensor (D). The vacuum pressure which impacts the mechanism stiffness is generated and regulated by the vacuum generator (E) and monitored by the pressure gauge (F).

from 10-mil polyurethane film. The polyurethane tube is cut and attached perpendicular to the film with vinyl cement, HH-66. On the final assembly, T-slot nuts are used to secure the beams to the end blocks.

6.2. Stiffness measurement

The experiment setup is shown in Fig. 10. The mechanism is secured to the optical table. The force sensor (resolution: 0.05N) is placed against the distal end. The force sensor coupled with the displacement sensor (resolution: 0.01mm) collect force versus deflection data, while the mechanism deflects from its initial position to a tip deflection of 20mm. Multiple data collections are made from 0 psi (0 Pa) to 12.5 psi (86.2 kPa) with an increment of 2.5 psi (17.2 kPa).

The experimental data shown in Fig. 11 exhibit three loading phases, consistent with the FEA prediction. For non-zero pressures, the lateral stiffness initially keeps constant at 6.05 N/mm (Phase I), then decreases (Phase II) to a lower value (Phase III). In the case when vacuum pressure is not applied, the external load increases linearly with tip deflection producing constant stiffness at 0.0803 N/mm. This is due to the layer material's low stiction characteristic that minimizes the

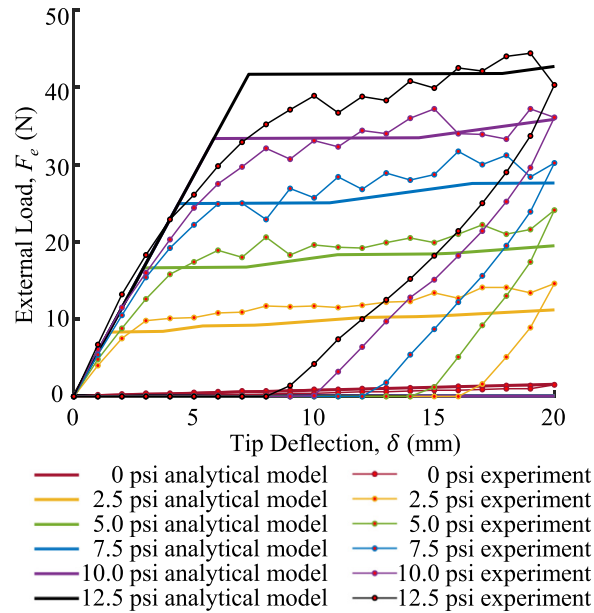


Fig. 11. Comparison between the theoretical and experimental results of external load vs. tip deflection relationship.

jamming effect under zero pressure. If high stiction material such as sandpaper is used, adhesion occurs between layers even if no vacuum pressure is applied. This gives a higher zero-pressure stiffness, which adversely impacts the stiffness ratio. Load-deflection data are also collected in the unloading process. The mechanism tends to restore its initial position due to the stored strain energy in the flexible backbone. At zero pressure, as the external force is gradually reduced, the mechanism completely recovers its initial position. As discussed, this is mainly due to the low stiction of the selected layer material. With vacuum pressure applied, the unloading curves exhibit typical hysteretic behavior, i.e., a residual distal deflection is observed. Higher vacuum pressure leads to a higher degree of hysteresis which is exemplified by larger residual distal deflection.

Compared with the experimental data, the analytical model predicts Phase I and Phase III stiffness variations for non-zero pressures and a constant stiffness under zero pressure. The analytical and experimental curves differ in two aspects. First, the analytical curve exhibits a clear deflection point rather than a smooth transition phase (Phase II) on the experimental curve. This might be caused by the analytical model's assumption for simplification that the boundary between slip- and non-slip regions applies to all of the layers. The boundaries may differ for different layers. Second, the experimental curves show a zigzag pattern in Phase III. It is speculated that the zigzag pattern is related to the typical stick-slip motion when two objects are in contact. A more sophisticated friction model is needed to more precisely simulate this behavior. Another error may be introduced by the manufacturing method of the beam. 3D-printed materials do not behave like solid materials since the material is fused-deposited layer by layer and has porous infill structures.

Simple state that 3D-printed materials do not behave like solid materials. That will contribute to the error between the FEA and prototype testing results. Testing validation was restricted to 3D-printed materials but mechanisms manufactured from solid materials should eliminate the error induced by 3D-printing. This should be discussed when discussing the results from the test (like those shown in Fig. 11). The agreement is relatively good as is so no large discussion is needed so the comments about optimizing printing settings is not needed, just a general statement that 3D-printing materials will introduce some error.

The analytical model explicitly incorporates fundamental design parameters including geometrical dimensions, material properties for both jamming layers and center beams, the number of jamming layers, the external load, and the applied vacuum pressure.

At 0 psig vacuum pressure, the mechanism's stiffness is defined as the base stiffness, which is used to calculate the stiffness ratio. The base stiffness characterizes the flexibility of the center backbone. Then under various vacuum pressures, the thin material that was attached to center beams is pressed, thereby generating a friction force that resists the beam deflection. The stiffness increases as the applied vacuum pressure is increased. The stiffness ratio is calculated as the stiffness corresponding to 12.5 psig divided by the base stiffness. The experiment on the prototype shows that a stiffness ratio by 75 times is achieved.

7. Conclusions

This study demonstrates, theoretically and experimentally, that layer jamming, combined with parallel-guided beams, is an effective approach in varying stiffness of compliant mechanisms. The novelty of the proposed compliant mechanism is

that each beam of the parallel-guided structure is a compliant backbone, combined with the layer jamming mechanism. The compliant backbone serves two purposes: (1) to significantly increase the mechanism's stiffness ratio due to the backbone structure's large thickness and (2) to restore the mechanism to its undeflected shape upon releasing the vacuum pressure. Our experiments show that this design achieves an exceptional high stiffness ratio by 75, at a very high response speed. However this is at the cost of reduced compactness. In addition to the novel design mentioned above, the main contributions of this work include: (1) an analytical kinetostatic model is developed to quantify structural stiffness in terms of design parameters; (2) critical design parameters are identified for maximizing the effect of stiffness ratio, which provides a guideline for high stiffness ratio design on similar structures; (3) a comprehensive solution is proposed, including the internal air channels and high-flow-rate vacuum generator, that significantly improves the response; (4) the stability of parallel-guided configuration is analyzed.

Acknowledgments

This material is based upon work supported by the [National Science Foundation](#) under Grant No. [CMMI-1637656](#). Any opinions, findings, and conclusions or recommendations expressed in this material are those of the author(s) and do not necessarily reflect the views of the funding agencies.

References

- [1] D. Rus, M.T. Tolley, Design, fabrication and control of soft robots, *Nature* 521 (7553) (2015) 467–475, doi:[10.1038/nature14543](#).
- [2] D. Trivedi, C.D. Rahn, W.M. Kier, I.D. Walker, Soft robotics: biological inspiration, state of the art, and future research, *Appl. Bionic. Biomech.* 5 (3) (2008) 99–117, doi:[10.1080/11762320802557865](#).
- [3] R. Wood, C. Walsh, Smaller, Softer, Safer, Smarter Robots, *Sci. Transl. Med.* 5 (210) (2013), 210ed19–210ed19, doi: [10.1126/scitranslmed.3006949](#).
- [4] L. Blanc, A. Delchambre, P. Lambert, Flexible medical devices: review of controllable stiffness Solutions, *Actuators* 6 (3) (2017) 23, doi:[10.3390/act6030023](#).
- [5] Y. She, H.-J. Su, C. Lai, D. Meng, Design and Prototype of a Tunable Stiffness Arm for Safe Human-Robot Interaction, in: Volume 5B: 40th Mechanisms and Robotics Conference, ASME, Charlotte, North Carolina, USA, 2016. V05BT07A063, doi: [10.1115/DETC2016-59523](#).
- [6] B.E. Schubert, D. Floreano, Variable stiffness material based on rigid low-melting-point-alloy microstructures embedded in soft poly(dimethylsiloxane) (PDMS), *RSC Adv.* 3 (46) (2013) 24671, doi: [10.1039/c3ra44412k](#).
- [7] S.S. Sun, Y. Chen, J. Yang, T.F. Tian, H.X. Deng, W.H. Li, H. Du, G. Alici, The development of an adaptive tuned magnetorheological elastomer absorber working in squeeze mode, *Smart Mater. Struct.* 23 (7) (2014) 075009, doi: [10.1088/0964-1726/23/7/075009](#).
- [8] S. Hauser, M. Robertson, A. Ijspeert, J. Paik, Jammjoint: a variable stiffness Device Based on Granular Jamming for Wearable Joint Support, *IEEE Robot. Automat. Lett.* 2 (2) (2017) 849–855, doi:[10.1109/LRA.2017.2655109](#).
- [9] E. Brown, N. Rodenberg, J. Amend, A. Mozeika, E. Steltz, M.R. Zakin, H. Lipson, H.M. Jaeger, Universal robotic gripper based on the jamming of granular material, *Proc. Natl. Acad. Sci.* 107 (44) (2010) 18809–18814, doi: [10.1073/pnas.1003250107](#).
- [10] N.G. Cheng, M.B. Lobovsky, S.J. Keating, A.M. Setapen, K.I. Gero, A.E. Hosoi, K.D. Iagnemma, Design and analysis of a robust, low-cost, highly articulated manipulator enabled by jamming of granular media, in: 2012 IEEE International Conference on Robotics and Automation, IEEE, St Paul, MN, USA, 2012, pp. 4328–4333, doi: [10.1109/ICRA.2012.6225373](#).
- [11] A. Jiang, G. Xynogalas, P. Dasgupta, K. Althoefer, T. Nanayakkara, Design of a variable stiffness flexible manipulator with composite granular jamming and membrane coupling, in: 2012 IEEE/RSJ International Conference on Intelligent Robots and Systems, IEEE, Vilamoura-Algarve, Portugal, 2012, pp. 2922–2927, doi: [10.1109/IROS.2012.6385696](#).
- [12] T. Ranzani, M. Cianchetti, G. Gerboni, I.D. Falco, G. Petroni, A. Menciassi, A modular soft manipulator with variable stiffness4.
- [13] T. Ranzani, M. Cianchetti, G. Gerboni, I.D. Falco, A. Menciassi, A soft modular manipulator for minimally invasive surgery: design and characterization of a single Module, *IEEE Trans. Robot.* 32 (1) (2016) 187–200, doi: [10.1109/TRO.2015.2507160](#).
- [14] M. Brancadoro, M. Manti, S. Tognarelli, M. Cianchetti, Preliminary experimental study on variable stiffness structures based on fiber jamming for soft robots, in: 2018 IEEE International Conference on Soft Robotics (RoboSoft), IEEE, Livorno, 2018, pp. 258–263, doi: [10.1109/ROBOSOFT.2018.8404929](#).
- [15] J. Ou, L. Yao, D. Tauber, J. Steimle, R. Niiyama, H. Ishii, jamSheets: thin interfaces with tunable stiffness enabled by layer jamming, in: Proceedings of the 8th International Conference on Tangible, Embedded and Embodied Interaction - TEI '14, ACM Press, Munich, Germany, 2013, pp. 65–72, doi: [10.1145/2540930.2540971](#).
- [16] Y.-J. Kim, S. Cheng, S. Kim, K. Iagnemma, Design of a tubular snake-like manipulator with stiffening capability by layer jamming, in: 2012 IEEE/RSJ International Conference on Intelligent Robots and Systems, IEEE, Vilamoura-Algarve, Portugal, 2012, pp. 4251–4256, doi: [10.1109/IROS.2012.6385574](#).
- [17] Y. Kim, S. Cheng, S. Kim, K. Iagnemma, A novel layer jamming mechanism with tunable stiffness capability for minimally invasive surgery, *IEEE Trans. Robot.* 29 (4) (2013) 1031–1042, doi: [10.1109/TRO.2013.2256313](#).
- [18] M. Langer, E. Amanov, J. Burgner-Kahrs, Stiffening sheaths for continuum robots, *Soft Robot.* 5 (3) (2018) 291–303, doi: [10.1089/soro.2017.0060](#).
- [19] V. Wall, R. Deimel, O. Brock, Selective stiffening of soft actuators based on jamming, in: 2015 IEEE International Conference on Robotics and Automation (ICRA), 2015, pp. 252–257, doi: [10.1109/ICRA.2015.7139008](#).
- [20] J.L.C. Santiago, I.S. Godage, I.D. Walker, Soft robots and kangaroo Tails: modulating compliance in continuum Structures via Mechanical Layer Jamming18.
- [21] A.R. Deshpande, Z.T.H. Tse, H. Ren, Origami-inspired bi-directional soft pneumatic actuator with integrated variable stiffness mechanism, in: 2017 18th International Conference on Advanced Robotics (ICAR), IEEE, Hong Kong, China, 2017, pp. 417–421, doi: [10.1109/ICAR.2017.8023642](#).
- [22] S.M. Hadi Sadati, Y. Noh, S. Elnaz Naghibi, A. Kaspar, T. Nanayakkara, Stiffness control of soft robotic manipulator for minimally invasive surgery (MIS) Using Scale Jamming, in: H. Liu, N. Kubota, X. Zhu, R. Dillmann, D. Zhou (Eds.), *Intelligent Robotics and Applications*, 9246, Springer International Publishing, Cham, 2015, pp. 141–151, doi: [10.1007/978-3-319-22873-0_13](#).
- [23] S. Tognarelli, M. Brancadoro, V. Dolosor, A. Menciassi, Soft tool for gallbladder retraction in minimally invasive surgery based on layer jamming, in: 2018 7th IEEE International Conference on Biomedical Robotics and Biomechatronics (Biorob), IEEE, Enschede, 2018, pp. 67–72, doi: [10.1109/BIOROB.2018.8488152](#).
- [24] E. Amanov, T.-D. Nguyen, S. Markmann, F. Imkamp, J. Burgner-Kahrs, Toward a flexible variable stiffness endoport for single-site partial nephrectomy, *Annal. Biomed. Eng.* 46 (10) (2018) 1498–1510, doi: [10.1007/s10439-018-2060-4](#).
- [25] Y.S. Narang, J.J. Vlassak, R.D. Howe, Mechanically versatile soft machines through laminar jamming, *Adv. Funct. Mater.* 28 (17) (2018) 1707136, doi: [10.1002/adfm.201707136](#).
- [26] Y.S. Narang, A. Degirmenci, J.J. Vlassak, R.D. Howe, Transforming the dynamic response of robotic structures and systems through laminar jamming, *IEEE Robot. Automat. Lett.* 3 (2) (2018) 688–695, doi: [10.1109/LRA.2017.2779802](#).
- [27] R.J. Roark, W.C. Young, R.G. Budynas, *Roark's formulas for stress and strain*, 7th ed, McGraw-Hill, New York, 2002.